An experimental study of turbulent two-phase flow in hydraulic jumps and application of a triple decomposition technique — Source link ⧉

Hang Wang, Stefan Felder, Stefan Felder, Hubert Chanson

Institutions: University of Queensland, University of New South Wales

Published on: 11 Jul 2014 - Experiments in Fluids (Springer Berlin Heidelberg)

Topics: K-epsilon turbulence model, K-omega turbulence model, Turbulence modeling, Turbulence kinetic energy and Reynolds decomposition

Related papers:

- Experimental study of the air–water shear flow in a hydraulic jump

- Optical fibre probe measurements of bubbly flow in hydraulic jumps

- Structure of flow in hydraulic jumps

- Air–water flows down stepped chutes: turbulence and flow structure observations

- Air–water interface dynamic and free surface features in hydraulic jumps

An experimental study of turbulent two-phase flow in hydraulic jumps and application of a triple decomposition technique

Hang Wang ([1]) (*), Stefan Felder ([1,2]) and Hubert Chanson ([1])
([1]) The University of Queensland, School of Civil Engineering, Brisbane QLD 4072, Australia
([2]) Currently: The University of New South Wales, Sydney NSW 2052, Australia
(*) Corresponding author: hang.wang@uqconnect.edu.au

Abstract

Intense turbulence develops in the two-phase flow region of hydraulic jump, with a broad range of turbulent length and time scales. Detailed air-water flow measurements using intrusive phase-detection probes enabled turbulence characterisation of the bubbly flow, although the phenomenon is not a truly random process because of the existence of low-frequency, pseudo-periodic fluctuating motion in the jump roller. This paper presents new measurements of turbulent properties in hydraulic jumps, including turbulence intensity, longitudinal and transverse integral length and time scales. The results characterised very high turbulent levels and reflected a combination of both fast and slow turbulent components. The respective contributions of the fast and slow motions were quantified using a triple decomposition technique. The decomposition of air-water detection signal revealed 'true' turbulent characteristics linked with the fast, microscopic velocity turbulence of hydraulic jumps. The high-frequency turbulence intensities were between 0.5 and 1.5 close to the jump toe, and maximum integral turbulent length scales were found next to the bottom. Both decreased in the flow direction with longitudinal turbulence dissipation. The results highlighted the considerable influence of hydrodynamic instabilities of the flow on the turbulence characterisation. The successful application of triple decomposition technique provided the means for the true turbulence properties of hydraulic jumps.

Keywords

Hydraulic jump, Turbulence, Air-water flow measurement, Triple decomposition, Free-surface dynamics

List of symbols

C	Time-averaged void fraction
$\overline{C}$	Decomposed time-averaged void fraction of average signal component
C'	Decomposed time-averaged void fraction of low-frequency signal component
C"	Decomposed time-averaged void fraction of high-frequency signal component
C_{max}	Maximum time-averaged void fraction in the shear flow region
c	Instantaneous void fraction
$\overline{c}$	Decomposed instantaneous void fraction of average signal component
c'	Decomposed instantaneous void fraction of low-frequency signal component
c"	Decomposed instantaneous void fraction of high-frequency signal component
d_1	Inflow water depth immediately upstream of the jump toe [m]
d_2	Downstream water depth [m]
F	Bubble count rate [Hz]
$\overline{F}$	Decomposed bubble count rate of average signal component [Hz]
F'	Decomposed bubble count rate of low-frequency signal component [Hz]
F"	Decomposed bubble count rate of high-frequency signal component [Hz]
F_{max}	Maximum bubble count rate in the shear flow region [Hz]

Fr_1	Inflow Froude number, $Fr_1 = V_1 / \sqrt{g \times d_1}$
g	Gravity acceleration [m/s^2]
h	Upstream gate opening [m]
L_r	Length of jump roller [m], defined as the distance over which the free surface level increased monotonically
L_X	Longitudinal integral turbulent length scale [m]
L_X'	Decomposed longitudinal integral turbulent length scale of low-frequency signal component [m]
L_X''	Decomposed longitudinal integral turbulent length scale of high-frequency signal component [m]
$(L_X'')_{max}$	Maximum decomposed longitudinal integral turbulent length scale of high-frequency signal component [m]
L_{xx}	Advection length scale [m]
L_{xx}'	Decomposed advection length scale of low-frequency signal component [m]
L_{xx}''	Decomposed advection length scale of high-frequency signal component [m]
L_Z	Transverse integral turbulent length scale [m]
Q	Flow rate [m^3/s]
R_{xx}	Normalised auto-correlation function
$R_{xx'}$	Normalised cross-correlation function between leading and trailing phase-detection probe signals
R_{xx}''	Decomposed cross-correlation function between high-frequency signal component
R_{xz}	Normalised cross-correlation function between side-by-side phase-detection probe signals
Re	Reynolds number, $Re = \rho \times V_1 \times d_1 / \mu$
T	Time lag for maximum cross-correlation coefficient [s]
T'	Time lag for maximum decomposed cross-correlation function of low-frequency signal component [s]
T''	Time lag for maximum decomposed cross-correlation function of high-frequency signal component [s]
T_X	Longitudinal integral turbulent time scale [s]
T_X'	Decomposed longitudinal integral turbulent time scale of low-frequency signal component [s]
T_X''	Decomposed longitudinal integral turbulent time scale of high-frequency signal component [s]
$(T_X'')_{max}$	Maximum longitudinal integral turbulent time scale of high-frequency signal component [s]
$(T_X'')_{mean}$	Depth-averaged longitudinal integral turbulent time scale of high-frequency signal component [s]
T_{xx}	Auto-correlation time scale [s]
T_{xx}'	Decomposed auto-correlation time scale of low-frequency signal component [s]
T_{xx}''	Decomposed auto-correlation time scale of high-frequency signal component [s]
$T_{xx'}$	Longitudinal cross-correlation time scale [s]
$T_{xx'}'$	Decomposed longitudinal cross-correlation time scale of low-frequency signal component [s]
$T_{xx'}''$	Decomposed longitudinal cross-correlation time scale of high-frequency signal component [s]

T_{xz}	Transverse cross-correlation time scale [s]
T_Z	Transverse integral turbulent time scale [s]
$T_{0.5}$	Time lag for maximum auto-correlation coefficient [s]
Tu	Turbulence intensity
Tu'	Decomposed turbulence intensity of low-frequency signal component
Tu"	Decomposed turbulence intensity of high-frequency signal component
V	Average air-water interfacial velocity [m/s]
V'	Decomposed interfacial velocity of low-frequency signal component [m/s]
V"	Decomposed interfacial velocity of high-frequency signal component [m/s]
V_1	Average inflow velocity [m/s]
v'	Standard deviation of interfacial velocity [m/s]
W	Channel width [m]
x	(1) Longitudinal distance from the upstream gate [m]
	(2) Signal of leading sensor of phase-detection probe
x'	Signal of trailing sensor of phase-detection probe
x_1	Longitudinal position of jump toe [m]
Y_{90}	Characteristic elevation where C = 0.9 [m]
y	Vertical distance from the channel bed [m]
Δx	Longitudinal separation distance between two phase-detection probe sensors [m]
Δz	Transverse separation distance between two phase-detection probe sensors [m]
μ	Dynamic viscosity [Pa×s]
ρ	Density [kg/m³]
τ	Time lag [s]
$\tau_{0.5}$	Time lag between maximum and half maximum cross-correlation coefficient [s]

1 Introduction

A hydraulic jump is a sudden transition from a supercritical to subcritical flow, with discontinuity in flow depth as well as in pressure and velocity field at the transition point (Leutheusser & Kartha 1972, Hager 1992). It is '*a phenomenon of common occurrence in natural streams as well as of practical significance in hydraulic engineering projects*' (Lighthill 1978). The transition point where the upstream flow impinges into the downstream region is called the jump toe, and the flow region immediately downstream of jump toe, often seen with flow recirculation, is known as the jump roller. The flow in the jump roller is extremely complex, associated with uncontrolled exchange of air and water through the free-surface and air entrainment at the jump toe (Rajaratnam 1967, Montes 1998). Large-scale turbulence develops both at the free-surface and inside the roller, characterising self-sustained instabilities. The fluctuating nature of the flow such as oscillations of jump toe position and production of large eddies are visible in pseudo-periodic manners (Hoyt & Sellin 1989, Long et al. 1990). Microscopic turbulence exists meanwhile with much smaller time and length scales and mostly in randomness. Both macroscopic and microscopic turbulence properties interact with the entrainment and transport of air, leading to turbulence modulation by air bubbles. Considering of the numerous parameters required to describe the turbulent two-phase flow and the complexity arising with the coupling between almost all physical processes in wide ranges of length and time scales, our knowledge on hydraulic jumps is far from a full understanding. Physical modelling is to date the most reliable method for the study of this phenomenon, and recent development in numerical modelling of such breaking open channel flows requires solid

verification by supportive experimental data (Prosperetti & Tryggvason 2009, Lubin & Glockner 2013).

Direct measurements of air-water flow in hydraulic jump dated back to Rajaratnam (1962) who measured the void fraction and velocity distributions. Key contributions included but not limited to the work of Resch & Leutheusser (1972) highlighting the importance of inflow conditions and Chanson (1995) proposing an analogy of the air entrainment process in hydraulic jump with that in plunging jets. These experimental studies were facilitated with intrusive conductivity and hot-film anemometer phase-detection probes. The application of non-intrusive flow measurement techniques is limited to weak hydraulic jumps because most instruments are designed for mono-phase flow. For example, Svendsen et al. (2000) used laser Doppler velocimetry (LDV) on hydraulic jumps with Froude numbers smaller than 1.6, Lennon & Hill (2006) applied particle image velocimetry (PIV) to jumps in the Froude number range 1.4 to 3, and micro acoustic Doppler velocimetry (ADV) was used by Liu et al. (2004) and Mignot & Cienfuegos (2010) with the largest Froude numbers being 3.3 and 2 respectively. For the strong hydraulic jumps with presence of large amount of air bubbles, the non-intrusive techniques were mostly restricted to imaging of full-field air distributions (Mossa & Tolve 1998, Leandro et al. 2012). Detailed turbulence characteristics were mainly derived based upon intrusive air-water interface detections and statistical data analysis (Chanson & Toombes 2002). Correlation analysis of two-point phase-detection signals enabled successful quantification of turbulence intensity and further turbulent length/time scales in the high-velocity bubbly flow (Chanson & Carosi 2007). However, because the statistical data processing does not discriminate the large-scale non-randomness in the flow motion, the characterisation of micro-scale turbulence in hydraulic jump is adversely affected by the flow instabilities which are associated with the pseudo-periodic motions of free-surface and large vortical structures.

The most relevant studies of self-sustained flow instabilities were primarily focused on the free-surface dynamics. Previous experimental investigations encompassed Mouaze et al. (2005), Murzyn et al. (2007), Murzyn & Chanson (2009) and Chachereau & Chanson (2011). In their measurements, either intrusive wire gauges or non-intrusive acoustic displacement meters were used to analyse the surface fluctuations and characteristic frequencies. The translation of hydraulic jump position was examined by Mossa (1999), and observation of jump toe oscillation was reported in Zhang et al. (2013). A recent numerical simulation was conducted by Richard & Gavrilyuk (2013) modelling the free-surface fluctuations and jump toe oscillations. The computational results further indicated jump toe oscillation frequencies independent of the distance to the downstream boundary (Richard 2013). Relevant literature is also noticed in the field of breaking waves which are often modelled as travelling jumps (Lighthill 1978, Peregrine & Svendsen 1978) For example, Cox & Shin (2003) performed simultaneous measurements of void fraction and turbulence in the bore region of waves. The unsteadiness in pressure field beneath a hydraulic jump may be also linked with the interactions between vortical flow structures and the invert as well as the vertical velocity turbulence (Yan & Zhou 2006, Lopardo & Romagnoli 2009). A correlation between the turbulence intensity and a pressure fluctuation coefficient was proposed by Lopardo (2013). Further multiple correlations were enabled by simultaneous velocity, two-phase flow and free-surface measurements. Longo (2010,2011) investigated the coupling between turbulence intensity and free-surface turbulence in some weak, submerged hydraulic jumps with limited surface breaking. The relationship between roller surface deformation and air entrainment was discussed by Wang & Chanson (2014). To date no investigation considered the impact of flow instabilities on turbulence characterisation for strong hydraulic jumps with substantial air entrainment and intense free-surface deformation.

This paper presents new experiments of air-water flow and turbulence measurements using phase-detection probes. Turbulence properties were deduced from interfacial detection signals, including the turbulence intensity, correlation time scales, advection length scale, and integral turbulent length and time scales in both longitudinal and transverse directions. The experimental data showed some unusual large turbulent levels and turbulent scales, which was believed to be linked with the pseudo-periodic motions of the flow. Felder & Chanson (2014) observed similar unsteady motions in air-water flows on a pooled stepped spillway. They developed a triple decomposition technique for non-stationary air-water flows and were able to identify the true turbulent scales of the flow. Herein the triple decomposition technique was applied to the hydraulic jump flow to quantify the turbulent flow contributions linked with the fast and slow fluctuating velocity components. The results validated the application of this technique to hydraulic jump, and showed significant influence of the flow instabilities. The findings provided an improved quality of turbulence characterisation and a further insight into such a complex air-water flow.

2 Experimental instrumentation and data processing

2.1 Facility and instrumentation

Hydraulic jumps were generated in a 3.2 m long horizontal channel with a rectangular cross section of 0.5 m wide × 0.41 m high. Water was supplied from a constant head reservoir into the upstream head tank of the channel (Fig 1). The flow rate was measured with a Venturi meter in the supply line. An undershoot rounded gate (Ø = 0.3 m) in the head tank induced a horizontal impinging flow into the flume, and the downstream flow conditions were controlled with an overshoot sluice gate at the end of the channel. The inflow depth d_1 was measured with a pointer gauge.

The presence of large amount of air bubbles hindered the application of most non-intrusive turbulence measurement techniques. A robust instrument, successfully used for decades, is the intrusive conductivity phase-detection probe (Rajaratnam 1962, Chanson & Carosi 2007). The phase-detection probes were equipped with two needle sensors with an inner diameter of 0.25 mm (Fig 2). The two sensors were sampled simultaneously at 20 kHz for 45 s. Measurements were performed at various elevations y/d_1 and several vertical cross sections with longitudinal positions $(x-x_1)/d_1$ in the bubbly flow. The elevation of phase-detection probe was controlled with an electromagnetic digital scale.

The accuracy of the experiment relied largely upon the determination of inflow depth and mean jump toe position. While the Venturi meter provided an accuracy of ±2% for the flow rate measurement, the free-surface roughness of the impinging flow introduced uncertainties up to ±5% to the inflow depth measurement. The mean position of the oscillating jump toe was determined visually, with an expected accuracy of 0.01 m for the most turbulent hydraulic jumps. That corresponded to a largest uncertainty up to 12% for the positioning of the first longitudinal measurement location.

2.2 Basic signal processing

The phase-detection probe signal exhibited a bimodal voltage probability distribution, with two distinctive peaks corresponding to the detection of air and water phases respectively. An air-water threshold was selected at 50% between the two peak voltage probabilities, and all sample points in the raw signal were converted to instantaneous void fraction c, where c = 0 for water and c = 1 for air. The time-averaged void fraction C represented the volume of air per unit volume of air and

water, and the bubble count rate F, defined as the number of air bubbles or water droplets per unit time, was deduced.

When the two sensors of phase-detection probe were aligned with the flow direction and separated with a longitudinal distance Δx between the tips (Fig 2a), statistical turbulence properties were derived based upon some correlation analysis of the probe signals. Denoting the leading sensor signal as x and the trailing sensor signal as x', Figure 3 sketches typical shapes of the auto-correlation function $R_{xx}(\tau)$ for the leading signal and cross-correlation function $R_{xx'}(\tau)$ between the leading and trailing signals, where τ is the time lag between the correlated datasets, T is the time lag of maximum cross-correlation coefficient, $T_{0.5}$ and $\tau_{0.5}$ are respectively the relative time lags of half maximum auto-correlation and cross-correlation, i.e. $R_{xx}(T_{0.5}) = 0.5$ and $R_{xx'}(T+\tau_{0.5}) = (R_{xx'})_{max}/2$. The time-averaged air-water interfacial velocity, considered equivalent to the flow velocity, was calculated as:

$$V = \frac{\Delta x}{T} \tag{1}$$

Herein the time lag T indicated the average interfacial travel time between the sensor tips. The turbulence intensity $Tu = v'/V$ was estimated within some key assumptions. First, it was assumed that the successive detection of air-water interfaces by the phase-detection probe was a true random process, thus the correlation functions followed a Gaussian distribution, yielding the standard deviations of the auto-correlation and cross-correlation functions as $T_{0.5}/1.175$ and $\tau_{0.5}/1.175$ respectively (Chanson & Toombes 2002). Second, it was assumed that the number of air-water interfaces n was infinitely large, and the average interfacial travel time T satisfied that

$$\frac{1}{T} \times \sqrt{\sum_{i=1}^{n} \left(t_i - T \right)^2 \bigg/ n^2} = \sqrt{\sum_{i=1}^{n} \left(\frac{t_i - T}{t_i} \right)^2 \bigg/ n^2} \tag{2}$$

where t_i (i = 1, …, n) is the instantaneous interfacial travel time. The right hand side of Equation (2) yielded the true turbulence intensity v'/V, while the approximation Tu was derived from the left hand side based upon the first assumption:

$$Tu = 0.851 \times \frac{\sqrt{\tau_{0.5}^2 - T_{0.5}^2}}{|T|} \tag{3}$$

Note that the estimate of Tu was dependent upon the broadening of cross-correlation function and hence was a function of the longitudinal separation of the phase-detection probe sensors Δx. Felder & Chanson (2014) developed a slightly different expression of turbulence intensity using the auto- and cross-correlation time scales. In the present study, the turbulence intensity was calculated based upon Equation (3).

An auto-correlation time scale T_{xx} and cross-correlation time scales $T_{xx'}$ and T_{xz} were calculated as:

$$T_{xx} = \int_{0}^{\tau(R_{xx}=0)} R_{xx}(\tau) \times d\tau \tag{4}$$

$$T_{xx'} = \int_{T}^{\tau(R_{xx'}=0)} R_{xx'}(\tau) \times d\tau \tag{5}$$

$$T_{xz} = \int_{\tau(R_{xz}=(R_{xz})_{max})}^{\tau(R_{xz}=0)} R_{xz}(\tau) \times d\tau \tag{6}$$

T_{xx} and $T_{xx'}$ are illustrated in Figure 3, while T_{xz} was derived from the cross-correlation function $R_{xz}(\tau)$ between the synchronous signals of two side-by-side phase-detection probe sensors with the same streamwise and vertical locations but a transverse separation Δz (Fig 2b). The auto-correlation time scale T_{xx} is a measure of the characteristic advective time of bubbly flow structures (e.g. eddies advecting the air-water interfaces) in the streamwise direction. It further gave the advection length scale L_{xx}:

$$L_{xx} = V \times T_{xx} \tag{7}$$

The advection length scale L_{xx} is a characteristic longitudinal size of advecting eddies (Chanson & Carosi 2007). The cross-correlation time scales $T_{xx'}$ and T_{xz} were functions of the probe tip separations Δx and Δz. When the measurements were repeated for a range of separation distances, the integral turbulent length and time scales were further calculated in the longitudinal direction:

$$L_X = \int_{0}^{\Delta x((R_{xx'})_{max}=0)} (R_{xx'})_{max} \times d(\Delta x) \tag{8}$$

$$T_X = \frac{1}{L_X} \times \int_{0}^{\Delta x((R_{xx'})_{max}=0)} (R_{xx'})_{max} \times T_{xx'} \times d(\Delta x) \tag{9}$$

and in the transverse direction:

$$L_Z = \int_{0}^{\Delta z((R_{xz})_{max}=0)} (R_{xz})_{max} \times d(\Delta z) \tag{10}$$

$$T_Z = \frac{1}{L_Z} \times \int_{0}^{\Delta z((R_{xz})_{max}=0)} (R_{xz})_{max} \times T_{xz} \times d(\Delta z) \tag{11}$$

The integral length and time scales give some measure of the inherent turbulent scales of large vortical structures in the longitudinal and transverse directions respectively (Chanson 2007, Chanson & Carosi 2007). In the flow region with separate and additive advection and diffusion processes, it would be expected that the advection and integral turbulent length scales are about equal in the longitudinal direction: $L_{xx} \approx L_X$.

2.3 Decomposition of turbulent signals

The respective contributions of slow and fast pseudo-periodic motions to the turbulence characterisation were identified with a triple decomposition of the phase-detection probe signal. The

voltage signal was decomposed into an average component, a low-frequency component corresponding to the slow fluctuations and a high-frequency component corresponding to the fast turbulent motions (Felder & Chanson 2014). The frequency thresholds between the signal components were identified based upon a series of experimental investigations on free-surface dynamics, spectral analysis of instantaneous void fraction signals and sensitivity studies. In the present study, the thresholds were set at 0.33 Hz between mean and slow motions and at 10 Hz between slow and fast motions. Decomposition of instantaneous void fraction was performed thereafter with low-pass, band-pass and high-pass filtering (Felder & Chanson 2014):

$$c = \bar{c} + c' + c'' \tag{12}$$

where $\bar{c}$ is a mean void fraction, c' and c'' are respectively the low-frequency and high-frequency components. Equation (12) led to the decomposition of time-averaged void fraction $C = \bar{C} + C' + C''$, for which $\bar{C} \approx C$ and $C' \approx C'' \approx 0$. For the selected frequency ranges, most bubble count rates satisfied the relationships $F'' \approx F$, $\bar{F} \approx F' \approx 0$.

The decomposition of correlation functions was a linear process. The decomposed correlation functions were proportional to the correlation functions between the filtered signal components, with absence of time-averaged components in the results (Felder 2013). Therefore, most turbulence properties were obtained for the filtered signal components with the decomposed correlation functions. The decomposed time-averaged velocities were given by $V' = \Delta x/T'$ and $V'' = \Delta x/T''$, where T' and T'' are time lags for the corresponding maxima of decomposed cross-correlation functions. The experimental data suggested $T' \sim T'' \approx T$ hence $V' \sim V'' \approx V$ (see the relevant data below). The correlation time scales can be expressed as the sum of the decomposed terms (e.g. $T_{xx} \approx T_{xx}' + T_{xx}''$, $T_{xx'} \approx T_{xx}' + T_{xx}''$), each term being integrated with the corresponding decomposed correlation functions. For the advection length scale and longitudinal integral turbulent length/time scales, the high-frequency components were calculated as:

$$L_{xx}'' = V'' \times T_{xx}'' \tag{13}$$

$$L_X'' = \int_0^{\Delta x((R_{xx'}'')_{max} = 0)} (R_{xx'}'')_{max} \times d(\Delta x) \tag{14}$$

$$T_X'' = \frac{1}{L_X''} \times \int_0^{\Delta x((R_{xx'}'')_{max} = 0)} (R_{xx'}'')_{max} \times T_{xx'}'' \times d(\Delta x) \tag{15}$$

where $(R_{xx'}'')_{max}$ is the maximum of decomposed cross-correlation function $R_{xx'}''$ which is proportional to the cross-correlation function between the high-frequency signal components. The low-frequency components were obtained in similar ways. Particularly, though the calculation of turbulence intensity Tu (Eq (3)) is non-linear, a decomposition of $Tu \approx Tu' + Tu''$ was applied, where the decomposed terms Tu' and Tu'' were calculated in the form of Equation (3) with relevant parameters derived from corresponding correlation functions.

2.4 Experimental flow conditions

Three inflow Froude numbers $Fr_1 = 3.8$, 5.1 and 7.5 were investigated with two intake aspect ratios $h/W = 0.04$ and 0.06, giving a factor 2 in terms of Reynolds number. Partially developed inflow conditions were applied to all experimental flows. Measurements were performed on the channel

centreline, through three to five vertical cross sections depending upon the length of jump. The flow conditions are summarised in Table 1. The longitudinal and transverse integral turbulent length/time scales were only obtained with repeated measurements for the flow condition $Fr_1 = 7.5$, $Re = 6.6 \times 10^4$ & h/W = 0.04. Different separation distances between phase-detection probe sensors, Δx in longitudinal and Δz in transverse direction, were applied and summarised in Table 2.

All experimental data were analysed with a data processing and triple decomposition software in Fortran. Details about the software can be found in Felder (2013).

3 Two-phase flow measurement results

3.1 Flow patterns and instabilities

The characteristic dimensions of hydraulic jump, including the ratio of conjugate depths d_2/d_1, the relative jump roller length L_r/d_1 and time-averaged free-surface profile, were found to be functions of the inflow Froude number and almost independent of the Reynolds number. The jump roller was primarily characterised with intense turbulence developing both at the free-surface and inside the roller, major air entrainment at the jump toe and convective transport of air bubbles in the turbulent shear region. Self-sustained instabilities were visible with free-surface fluctuations and splashing, downstream propagation of surface waves, longitudinal jump toe oscillations, fluctuations of transverse impingement perimeter, and successive formation of large-scale vortices in which the entrapped air was advected downstream. These pseudo-periodic motions are illustrated in a side-view image of jump roller in Figure 4 and in the video appendices (Online Resource 1 & 2). The motions interacted with each other, and all contributed to the low-frequency fluctuations of the flow. The characteristic frequencies were observed and measured with non-intrusive water surface detections in several previous studies (Chanson 2006,2010, Murzyn & Chanson 2009, Chachereau & Chanson 2011, Zhang et al. 2013, Wang & Chanson 2014). The findings are summarised in Table 3. All experimental data showed comparable frequency ranges for jump toe oscillations and vortex advections between 0.4 and 2 Hz, while the free-surface fluctuation frequencies were between 0.8 and 4 Hz. The Strouhal number of the jump toe frequencies $f \times d_1/V_1$ was suggested to decrease with increasing inflow Froude number (Wang & Chanson 2014).

Note that all comparative studies in Table 3 were performed with flumes of the same length, and the tailwater length downstream of jump roller had little impact on the frequencies of the fluctuating motions. The observations were consistent with the numerical simulations of Richard (2013), with channel lengths between 3.2 m and 20 m and Froude numbers from 6 to 11. It is however acknowledged that, for one experiment ($Fr_1 = 7.5$, $d_1 = 0.03$ m), the downstream end of the roller interacted with the tailwater gate, thus inducing some form of semi-confinement.

3.2 Basic air-water flow properties

The distributions of time-averaged void fraction C and bubble count rate $F \times d_1/V_1$ on the channel centreline are presented in Figures 5a and 5b for the aspect ratio h/W = 0.06. The roller surfaces are outlined at the elevation Y_{90} where C = 0.9. The void fraction reflected the extent of the flow aeration, while the bubble count rate was further linked with the number and average size of bubbles as well as the total air-water interfacial area, which was largely determined by the local shear stress. The data profiles highlighted two flow regions in the jump roller, namely the turbulent shear region on the bottom and the recirculation region above, the boundary in between being characterised with a trough void fraction (also a trough bubble count rate). Both void fraction and

bubble count rate exhibited local maxima in the shear flow, but at different elevations. The local maximum values C_{max} and F_{max}, as well as the depth-averaged values, decreased along the roller for each flow. Figure 5c shows their longitudinal decay which was associated with the de-aeration of the shear flow, and the decreasing rates were functions of the Froude number. Comparison between the experimental data with the same Froude number but different aspect ratios showed larger bubble count rate for a higher Reynolds number (not shown) because, for a given void fraction, the number of bubbles was determined by the shear stress linked with the turbulence level of the flow. In the free-surface recirculation region, the void fraction increased rapidly to unity, and a secondary peak in bubble count rate profile was shown for $C = 0.3$ to 0.5. The typical data distributions applied to all flow conditions and were consistent with the previous investigations (Murzyn & Chanson 2009, Chanson 2010, Chachereau & Chanson 2011).

Figures 6a and 6b present respectively the interfacial velocity and turbulence intensity distributions for the same flow conditions in Figures 5a and 5b. The velocity profiles showed positive velocity in the shear region with longitudinal deceleration and almost uniform negative velocity for the reversed free-surface flow. The turbulence intensity Tu increased monotonically with increasing elevation in the positive flow region. When the negative velocity started to appear (though the average velocity could be still positive), the turbulence level increased significantly, sometimes yielding physically meaningless turbulence intensities over 3 to 4. This was attributed to the inclusion of macroscopic free-surface dynamics in the microscopic turbulence characterisation. The instantaneous velocity fluctuations encompassed the variations caused by the free-surface deformations and the oscillations of jump toe position which were larger in length and time scales compared to the "true" velocity turbulence. Details were given with a signal decomposition and discussed later in this paper.

The correlation time scales are presented for a given flow condition ($Fr_1 = 7.5$, $Re = 6.6\times10^4$, $h/W = 0.04$) for briefness. Figure 7 shows the auto-correlation time scale T_{xx} together with the longitudinal cross-correlation time scale $T_{xx'}$ for two probe sensor separations Δx and the transverse cross-correlation time scale T_{xz} for two sensor separations Δz. Except for some smaller cross-correlation time scale T_{xz} given by a large transverse spacing $\Delta z = 17.1$ mm, all correlation time scales exhibited comparable data profiles in a vertical cross section, with gradual increase with increasing elevation from the channel bed into the free-surface region where significantly larger time scales were shown because of the impact of large-scale free-surface fluctuations. Similar data distributions were obtained for all other flow conditions.

3.3 Turbulent length and time scales

The longitudinal advection length scale L_{xx}, calculated with the auto-correlation time scale T_{xx} and interfacial velocity V (Eq (7)), are compared with the longitudinal integral turbulent length scale L_X given by the integration of characteristic lengths equalling Δx weighted by the corresponding maximum correlation coefficients (Eq (8)). The results are shown in Figure 8a. The transverse integral length scale L_Z is also presented. All dimensionless length scales were shown in the same order of magnitude ($\sim10^{-2}$ m). It indicated that turbulent structures of comparable sizes developed both along and perpendicular to the main flow direction.

In the mixing shear layer, turbulent flow structures of various dimensions formed and were advected. The advection length scale L_{xx} represented some average dimension of these advecting structures, while the integral turbulent length scale L_X provided a statistic measure over a range of characteristic sizes in the streamwise direction. Both length scales were closely linked with the entrained air bubbles carried in these vortical structures. In the shear flow, the experimental data

showed larger integral length scale L_X than the advection length scale L_{xx} within a short distance downstream of the jump toe. It implied strong advecting processes exerted on a wide range of eddy sizes, especially for the large-size turbulent structures. The diffusion process was highly affected by the advective transportation, implying that Taylor's hypothesis of $L_{xx} \approx L_X$ for separate and additive diffusion and advection processes was not satisfied. Close length scales were achieved at further downstream positions in the lower flow region, associated with dissipation of large turbulent structures and separation of advective and diffusive processes.

The integral turbulent time scales T_X and T_Z are presented in Figure 8b. Similar data distributions were shown between longitudinal and transverse time scales. The results gave a measure of characteristic time scales of the air advection in large turbulent structures, which were in an order of magnitude of 10^{-3} s in the lower shear region and of 10^{-2} s near the free-surface.

4 Application of triple decomposition technique

4.1 Presentation

The correlation analysis of raw phase-detection probe signals yielded large and scattered turbulent flow properties in the free-surface region linked to the effects of macroscopic free-surface dynamics (Fig 6, 7 & 8). A decomposition of the signals allowed identification of respective contributions of the low-frequency and high-frequency motions based upon given frequency thresholds between the mean, slow and fast fluctuating signal components.

The frequency thresholds were selected with reference to the characteristic frequency ranges of the pseudo-periodic motions in hydraulic jumps. Experimental observations and measurements suggested typical frequency ranges from 0.4 to 4 Hz for free-surface fluctuations, jump toe oscillations and large-size vortex advections (Table 3). The findings applied to a wide range of flow conditions. Further spectral analysis of the raw voltage output was conducted. The energy density of signal reflected the detection of air-water interfaces. Figure 9 presents a power spectral density function of the raw signal at the elevation of maximum void fraction C_{max} in the shear flow, indicating some characteristic frequencies at 0.4, 10.7 and 216 Hz. The characteristic frequencies indicated a higher frequency range between 10.7 and 216 Hz corresponding to the detection of most air bubbles, while the impacts of flow instabilities was reflected in a range between 0.4 and 10.7 Hz. For most flow conditions in the present study, these characteristic frequencies were seen at about 0.3 to 0.5, 10 to 15 and above 100 Hz depending upon the position in jump roller. Overall, both experimental investigations and spectral analysis suggested the frequencies of slow fluctuations in an order of magnitude of 10^{-1} to 1 Hz. Herein the lower and upper cut-off frequencies of the slow fluctuations were set at 0.33 and 10 Hz respectively. The selection was supported by a sensitivity study of cut-off frequencies by Felder (2013) for a similar hydraulic jump configuration.

The decomposition was performed by filtering the raw phase-detection probe signal with the selected cut-off frequencies. The time-averaged void fraction C and bubble count rate F were respectively in the frequency ranges of mean and high-frequency component, hence $C \approx \bar{C}$ and $F \approx F''$. Further decomposition of turbulence properties, including time-averaged interfacial velocity, turbulence intensity, correlation time scales, advection length scale and integral turbulent length and time scales, were achieved with the decomposed correlation functions of corresponding signal components, where the mean component did not appear and the slow and fast fluctuating components were denoted with single and double prime respectively.

4.2 Decomposition of velocity, turbulence intensity and correlation time scales

The decomposed terms of interfacial velocity V, namely V' for the low-frequency signal component and V" for the high-frequency component, were calculated using the average interfacial travel times (T' & T") deduced from the filtered signal components. Typical results are shown in Figure 10 for one flow rate and a given longitudinal position. A best fit wall jet solution is also plotted for comparison (Chanson 2010). For all flow conditions, V and V" were shown about identical, while the distribution of V' was relatively scattered. The coincidence between V and V" was linked to the sequential detection of air-water interfaces with two phase-detection probe sensors being a high-frequency process (Felder & Chanson 2014). For a flow velocity between 1 and 5 m/s, the typical interfacial travel time between the sensor tips (5 mm < Δx < 10 mm) was between 1 and 10 ms, corresponding to a characteristic frequency from 100 to 1000 Hz, one to two orders of magnitude higher than the upper decomposition cut-off frequency. On the other hand, the low-frequency signal component provided less accurate estimate of T' with a broad, flat peak in the decomposed cross-correlation function (not shown here).

The turbulence intensity was calculated for both high-frequency and low-frequency filtered signals. The results Tu" and Tu' are shown in Figure 11a and compared with the turbulence intensity Tu deduced from the raw signal. The raw signal and low-frequency signal component gave comparable turbulence intensities Tu $\approx$ Tu', with large values in the upper part of roller, whereas the high-frequency signal component yielded smaller, less scattered turbulence intensity Tu" through the vertical cross section. Tu" showed some constant level of magnitude in both shear flow and recirculation region. In a thin layer between the two flow regions, Tu" was larger, because the local flow direction changed frequently with successive advection of large vortices, and the time-averaged velocity was small and close to zero. The data distribution was typical in the first half roller for all flow conditions. Figure 11b plots all Tu and Tu" in the first half roller at the relative elevation y/Y_{90}, showing Tu" mainly between 0.5 and 1.5. Comparison between different flow conditions suggested Tu" increased with increasing Reynolds number but was almost independent of Froude number. The results were larger than the findings of Resch & Leutheusser (1972) and Liu et al. (2004) who measured turbulence intensities no larger than 0.8, though their Froude numbers were restricted between 2 and 6. In Figure 11b, a few scattered data points with large Tu" were seen in the upper flow region, because meaningless correlation functions were sometimes obtained for the raw signal, which could not be addressed by the signal decomposition technique. In the second half roller, Tu" decreased to between 0 and 0.7 as the high-frequency turbulence was largely dissipated.

Although the calculation of turbulence intensity is not a linear process, and the decomposition of turbulence intensity cannot be theoretically justified, the experimental results supported the relationship Tu $\approx$ Tu' + Tu". Further justification of the decomposition of turbulence intensity was given by Felder & Chanson (2014) by comparing stepped spillway flows with and without instabilities. Their study demonstrated comparable turbulence intensities deduced from the raw signal of the stable flow and the high-frequency signal component of the instable flow, thus the high-frequency signal component gave agreeable turbulence intensity with absence of the impact of flow instabilities.

Figure 12 shows the decomposed auto-correlation time scales and longitudinal cross-correlation time scales in the same cross section, with reference to the time-averaged void fraction profile. The cross-correlation time scales corresponded to a longitudinal spacing between the phase-detection probe sensors Δx = 7.12 mm. The time scales of high-frequency signal component (T_{xx}" & T_{xx}")

were shown significantly lower than those of raw signal (T_{xx} & $T_{xx'}$), especially in the upper flow region. The data satisfied the relationships $T_{xx} \approx T_{xx}' + T_{xx}''$ and $T_{xx'} \approx T_{xx'}' + T_{xx'}''$. For the given value of Δx, the decomposed cross-correlation time scale $T_{xx'}''$ was consistently smaller than the decomposed auto-correlation time scale T_{xx}'' at the same longitudinal position.

4.3 Decomposition of integral turbulent length and time scales

The triple decomposition technique was applied to the characterisation of longitudinal advection length scale and integral turbulent length and time scales for the fast and slow turbulent motions in hydraulic jump. Figure 13a presents the advection and integral turbulent length scales for both raw and filtered signals in the same cross section, including the void fraction profile. Both high-frequency decomposed length scales were significantly smaller than those of raw signal and low-frequency signal component, especially in the upper shear flow and entire free-surface region where each high-frequency length scale was nearly uniform. It implied that the large length scales of raw signal were mainly induced by the low-frequency motions in the flow, with the largest impact at the free-surface. In the lower shear flow, both high-frequency length scales exhibited maxima, $(L_{xx}'')_{max}$ and $(L_X'')_{max}$, and the integral length scale L_X'' was consistently larger than the advection length scale L_{xx}''. This is illustrated in Figure 13b. The shape of vertical distribution reflected the existence of high-frequency turbulent structures in the lower shear flow, which were rarely seen in the upper flow region. The low vertical positions of these turbulent structures were in agreement with the observations showing the interaction between the shielding of large vortices and channel bed. Figure 13b also showed decreases in both maximum length scales with increasing distance from the jump toe. The longitudinal decay of $(L_{xx}'')_{max}/d_1$ and $(L_X'')_{max}/d_1$ is shown in Figure 13c for the given flow condition ($Fr_1 = 7.5$, $Re = 6.6 \times 10^4$), with the data correlated as:

$$\frac{\left(L_{xx}''\right)_{max}}{d_1} = 0.28 \times \exp\left(-0.038 \times \frac{x\text{-}x_1}{d_1} \right) \qquad \text{for } Fr_1 = 7.5, Re = 6.6 \times 10^4 \quad (16)$$

$$\frac{\left(L_X''\right)_{max}}{d_1} = 0.79 \times \exp\left(-0.057 \times \frac{x\text{-}x_1}{d_1} \right) \qquad \text{for } Fr_1 = 7.5, Re = 6.6 \times 10^4 \quad (17)$$

Though the size of large vortices was observed to increase along the roller, the decreasing turbulent length scales indicated the dissipation of high-frequency turbulent structures which acted a more predominant role. L_{xx}'' and L_X'' were expected to be equal at further downstream positions in the quasi-uniform subcritical flow, and both ultimately decreased to zero as the high-frequency turbulence is fully dissipated.

The decomposition of length scales showed the relationships $L_{xx} \sim L_{xx}'+L_{xx}''$ and $L_X \approx L_X'+L_X''$. The scattered low-frequency advection length scale L_{xx}' was related to the scattered low-frequency velocity component V'. Comparison between the two length scales indicated different relationships in the upper and lower flow regions, i.e., $L_{xx} > L_X$, $L_{xx}' > L_X'$, $L_{xx}'' \approx L_X''$ for $y > y(C = C_{max})$, and $L_{xx} < L_X$, $L_{xx}' \approx L_X'$, $L_{xx}'' < L_X''$ for $0 < y < y(C = C_{max})$ (Fig 13a). It implied that the difference in the advection and integral length scales of raw signal was mainly caused by the slow fluctuations in the upper flow and by the fast turbulent motions in the lower flow region. In the lower shear flow, the larger integral length scale than advection length scale reflected strong and fast advection of relatively large turbulent structures in the longitudinal direction.

The decomposition of longitudinal integral turbulent time scale T_X showed comparable results to the decomposed correlation time scales (Fig 12). The results are plotted in Figure 14a, showing close integral time scales of raw and low-frequency signals ($T_X \approx T_X'$). The high-frequency integral time scale T_X'' was an order of magnitude smaller than T_X and T_X' in the upper flow region, and the data exhibited $T_X \approx T_X' + T_X''$. Figure 14b shows the distribution of T_X'' in detail, with comparison to the high-frequency auto- and cross-correlation time scales, T_{xx}'' and $T_{xx'}''$, at two longitudinal positions. The integral and cross-correlation time scales were shown with the same level of quantities and both smaller than the auto-correlation time scale in the same cross section. In the lower shear flow, the high-frequency integral time scale exhibited a maximum $(T_X'')_{max}$, which decreased in the streamwise direction. Figure 14c presents the maximum as well as depth-averaged integral time scales as functions of the longitudinal position. The data were correlated by:

$$\frac{(T_X'')_{max} \times V_1}{d_1} = 0.24 \times \exp\left(-0.02 \times \frac{x - x_1}{d_1}\right) \qquad \text{for } Fr_1 = 7.5, \ Re = 6.6 \times 10^4 \ (18)$$

$$\frac{(T_X'')_{mean} \times V_1}{d_1} = 0.196 \times \exp\left(-0.016 \times \frac{x - x_1}{d_1}\right) \qquad \text{for } Fr_1 = 7.5, \ Re = 6.6 \times 10^4 \ (19)$$

The longitudinal decrease in integral turbulent time scale characterised the shortening of a characteristic "lifetime" of high-frequency turbulent structures in the streamwise direction.

5 Conclusion

New experiments were conducted using dual-tip phase-detection probes to characterise the air-water flow properties in hydraulic jumps. The air-water interfacial velocity, turbulence intensity, correlation time scales, advection length scale and integral turbulent length and time scales were deduced from a statistical analysis of the probe signal. The turbulent length and time scales were seen quantitatively comparable in the longitudinal and transverse directions, highlighting the existence of transverse flow structures in the hydraulic jump roller, despite the pseudo-two-dimensional flow pattern.

High turbulence levels were recorded in the roller free-surface region that were linked to the existence of self-sustained instabilities. The hydrodynamic instabilities took place in the form of pseudo-periodic free-surface deformations and large-scale turbulent flow structures. Their characteristic frequencies were between 0.4 and 4 Hz. The influence of both low-frequency motion and high-frequency turbulence motion was quantified using a triple decomposition technique applied to the raw air-water detection signal. The frequency thresholds were set at 0.33 Hz and 10 Hz. The signal decomposition showed a significant reduction in turbulence intensity and characteristic turbulent scales for the high-frequency signal component. The turbulence intensity Tu'' was shown between 0.5 and 1.5 close to the jump toe and it decreased with increasing distance from the jump toe. The magnitude in 'true' turbulence levels was comparable to earlier studies. The high-frequency advection length scale and integral turbulent length scale exhibited some maxima in the lower shear flow next to the invert. The turbulent length scales decreased along the roller as the fast turbulence was dissipated. Comparison between the longitudinal advection and integral length scales indicated that the advection and diffusion were not independent processes in the flow region immediately downstream of the jump toe. All characteristic turbulent scales were decomposed between high-frequency and low-frequency contributions. The impact of slow fluctuations was large in the free-surface region and relatively smaller in the lower shear flow.

The present study demonstrated a successful application of the triple decomposition technique to the hydraulic jumps. The results successfully quantified the turbulence that was truly related to the random fast velocity fluctuations, hence highly improved the quality of turbulence characterisation. The estimate of turbulence properties in such turbulent two-phase flow based upon statistical analysis of air-water detection data was justified in the free-surface area outside the shear flow.

Online Resource: Video of non-stationary experimental hydraulic jumps

Two videos of the experimental hydraulic jumps are supplemented to illustrate the flow instabilities. The videos were taken with a digital video camera (25 fps) and hydraulic jumps were generated in a different horizontal channel with same dimensions to the one used in the present study. Online Resource 1 (Movie_top_Fr5.mpg) presents an overhead view of the jump, showing the longitudinal oscillations of jump toe position and fluctuations of transverse impingement perimeter. The flow conditions were: $Q = 0.0376$ m^3/s, $W = 0.5$ m, $h = 0.024$ m, $d_1 = 0.0283$ m, $x_1 = 1.0$ m, $Fr_1 = 5.0$, $Re = 7.5 \times 10^4$. Online Resource 2 (Movie_side_Fr5.mpg) provides a side view of the same flow, showing free-surface fluctuations, surface wave propagations and formation and advection of large eddies in the jump roller.

Acknowledgements

References

Chachereau Y, Chanson H (2011) Free-surface fluctuations and turbulence in hydraulic jumps. Exp Thermal Fluid Sci 35(6):896–909. doi:10.1016/j.expthermflusci.2011.01.009

Chanson H (1995) Air entrainment in two-dimensional turbulent shear flows with partially developed inflow conditions. J Multiphase Flow 21(6):1107-1121

Chanson H (2006) Air bubble entrainment in hydraulic jumps. similitude and scale effects. Academic Report No. CH57/05, Dept. of Civil Engineering, The University of Queensland, Brisbane, Australia

Chanson, H (2010) Convective transport of air bubbles in strong hydraulic jumps. International Journal of Multiphase Flow 36(10):798-814. doi:10.1016/j.ijmultiphaseflow.2010.05.006

Chanson H, Carosi G (2007) Turbulent time and length scale measurements in high-velocity open channel flows. Experiments in Fluids 42(3):385-401. doi:10.1007/s00348-006-0246-2

Chanson H, Toombes L (2002) Air-water flows down stepped chutes: turbulence and flow structure observations. International Journal of Multiphase Flow 28(11):1737-1761

Cox D, Shin S (2003) Laboratory measurements of void fraction and turbulence in the bore region of surf zone waves. J. Eng. Mech. 129:1197-1205

Felder S (2013) Air-water flow properties on stepped spillways for embankment dams: aeration, energy dissipation and turbulence on uniform, non-uniform and pooled stepped chutes. PhD thesis, School of Civil Engineering, The University of Queensland, Brisbane, Australia

Felder S, Chanson H (2014) Triple decomposition technique in air–water flows: application to instationary flows on a stepped spillway. International Journal of Multiphase Flow 58:139-153. doi:10.1016/j.ijmultiphaseflow.2013.09.006

Hager WH (1992) Energy dissipators and hydraulic jump. Kluwer Academic Publ, Water Science and Technology Library 8, Dordrecht, The Netherlands

Hoyt JW, Sellin RHJ (1989) Hydraulic Jump as 'Mixing Layer'. J Hydrolic Engineering, ASCE, 115(12):1607-1614

Leandro J, Carvalho R, Chachereau Y, Chanson H (2012) Estimating void fraction in a hydraulic jump by measurements of pixel intensity. Experiments in Fluids 52(5):1307-1318

Lennon JM, Hill DF (2006) Particle image velocity measurements of undular and hydraulic jumps. Journal of Hydraulic Engineering, ASCE 132(12):1283-1294

Leutheusser HJ, Kartha VC (1972) Effects of Inflow Condition on Hydraulic Jump. Jl of Hyd. Div., ASCE, 98(HY8):1367-1385

Lighthill J (1978) Waves in fluids. Cambridge University Press, Cambridge, UK

Liu M, Rajaratnam N, Zhu D (2004) Turbulence structure of hydraulic jumps of low Froude numbers. Journal of Hydraulic Engineering 130(6):511–520. doi:10.1061/(ASCE)0733-9429(2004)130:6(511)

Long D, Rajaratnam N, Steffler PM, Smy PR (1991) Structure of flow in hydraulic jumps. Journal of Hydraulic Research, IAHR 29(2):207-218

Longo S (2010) Experiments on turbulence beneath a free surface in a stationary field generated by a Crump weir: free-surface characteristics and the relevant scales. Experiments in Fluids, 49:1325-1338

Longo S (2011) Experiments on turbulence beneath a free surface in a stationary field generated by a Crump weir: turbulence structure and correlation with the free surface. Experiments in Fluids, 50:201-215

Lopardo RA (2013) Extreme velocity fluctuations below free hydraulic jumps. Journal of Engineering, Hindawi Publishing Corporation, Article ID 678065

Lopardo RA, Romagnoli M (2009) Pressure and velocity fluctuations in stilling basins. Advances in Water Resources and Hydraulic Engineering, Proceedings of 16th IAHR-APD Congress and 3rd IAHR International Symposium on Hydraulic Structures ISHS, Nanjing, China

Lubin P, Glockner S (2013) Detailed numerical investigation of the three-dimensional flow structures under breaking waves. 7th Conference on Coastal Dynamics, Arcachon, France, 24-28 June 2013. pp 1127-1136

Mignot E, Cienfuegos R (2010) Energy dissipation and turbulent production in weak hydraulic jumps. Journal of Hydraulic Engineering, ASCE 136(2):116-121

Montes JS (1998) Hydraulics of Open Channel Flow. ASCE Press, New York, USA

Mossa M (1999) On the oscillating characteristics of hydraulic jumps. Journal of Hydraulic Research, IAHR 37(4):541-558

Mossa M, Tolve U (1998) Flow visualization in bubbly two-phase hydraulic jump. Journal of Fluids Engineering, ASME 120:160-165

Mouaze D, Murzyn F, Chaplin JR (2005) Free surface length scale estimation in hydraulic jumps. Journal of Fluids Engineering, Transactions ASME 127:1191-1193. doi:10.1115/1.2060736

Murzyn F, Mouaze D, Chaplin JR (2007) Air-water interface dynamic and free surface features in hydraulic jumps. Journal of Hydraulic Research, IAHR 45(5):679-685

Murzyn F, Chanson H (2009) Experimental investigation of bubbly flow and turbulence in hydraulic jumps. Environmental Fluid Mechanics 9(2):143-159. doi:10.1016/j.expthermflusci.2009.06.003

Peregrine DH, Svendsen IA (1978) Spilling breakers, bores and hydraulic jumps. Proc. 16th Int. Conf. Coastal Eng., Hamburg, Germany

Prosperetti A, Tryggvason G (2009) Computational methods for multiphase flow. Cambridge University Press, London, UK

Rajaratnam N (1962) An experimental study of air entrainment characteristics of the hydraulic jump. Journal of Instruction Engineering India 42(7):247-273

Rajaratnam, N (1967) Hydraulic Jumps. Advances in Hydroscience, Ed. V.T. CHOW, Academic Press, New York, USA, 4, 197-280.

Resch FJ, Leutheusser HJ (1972) Le ressaut hydraulique: mesure de turbulence dans la région diphasique. Journal La Houille Blanche 4:279-293 (in French)

Richard GL (2013) Élaboration d'un modèle d'écoulements turbulents en faible profondeur: application au ressaut hydraulique et aux trains de rouleaux. PhD thesis, Institut Universitaire des Systèmes Thermiques Industriels, Univerité d'Aix-Marseille, Marseille, France (in French)

Richard GL, Gavrilyuk SL (2013) The classical hydraulic jump in a model of shear shallow-water flows. Journal of Fluid Mechanics 725:492-521. doi:10.1017/jfm.2013.174

Svendsen IA, Veeramony J, Bakunin J, Kirby JT (2000) The flow in weak turbulent hydraulic jumps. Journal of Fluid Mechanics, 418:25-57

Wang H, Chanson H (2014) Air entrainment and turbulent fluctuations in hydraulic jumps. Urban Water Journal. doi:10.1080/1573062X.2013.847464

Yan Z, Zhou C (2006) Pressure fluctuations beneath spatial hydraulic jumps. Journal of Hydrodynamics, 18(6):723-726

Zhang G, Wang H, Chanson H (2013) Turbulence and aeration in hydraulic jumps: free-surface fluctuation and integral turbulent scale measurements. Environmental Fluid Mechanics 13(2):189–204. doi:10.1007/s10652-012-9254-3

List of Tables

Table 1. Experimental flow conditions.

Q [m^3/s]	W [m]	h [m]	x_1 [m]	d_1 [m]	V_1 [m/s]	L_r [m]	Fr_1 [-]	Re [-]
0.0170	0.5	0.020	0.83	0.020	1.70	0.28	3.8	3.4×10^4
0.0226				0.020	2.26	0.52	5.1	4.5×10^4
* 0.0333				0.020	3.33	0.80	7.5	6.6×10^4
0.0342	0.5	0.030	1.25	0.032	2.14	0.60	3.8	6.8×10^4
0.0460				0.032	2.88	0.85	5.1	9.1×10^4
0.0706				0.033	4.28	1.45	7.5	1.4×10^5

Notes: Q: flow rate; W: channel width; h: upstream gate opening; x_1: longitudinal jump toe position; d_1: inflow depth; V_1: average inflow velocity; L_r: roller length Fr_1: inflow Froude number; Re: inflow Reynolds number; *: integral turbulent length/time scale measurements.

Table 2. Separation distances between two phase-detection probe sensor tips for the measurement of longitudinal and transverse integral turbulent scales with flow conditions Fr_1 = 7.5, Re = 6.6×10^4 and h/W = 0.04.

Turbulent properties	Δx [mm]	Δz [mm]
L_X, T_X	2.57, 5.0, 7.25, 9.28, 13.92, 29.68	2.0
L_Z, T_Z	0	0.9, 3.6, 9.0, 17.1, 27.0, 36.6, 49.2, 92.0

Notes: L_X, T_X: longitudinal integral turbulent length/time scale; L_Z, T_Z: transverse integral turbulent length/time scale; Δx, Δz: longitudinal/transverse separation distance between the phase-detection probe sensors.

Table 3. Characteristic frequency ranges of pseudo-periodic motions in hydraulic jump.

Motions of flow	Reference	Method	Frequency range [Hz]
Free-surface fluctuations	Murzyn & Chanson (2009)	ADM measurement	0.8 to 4.0
	Chachereau & Chanson (2011)	ADM measurement	1.6 to 3.9
	Wang & Chanson (2014)	ADM measurement	1.2 to 3.7
Jump toe oscillations	Chanson (2006)	visual observation	0.6 to 2.0
	Murzyn & Chanson (2009)	visual observation	0.5 to 0.8
	Chanson (2010)	visual observation	0.4 to 0.8
	Zhang et al. (2013)	visual observation	0.7 to 1.4
	Wang & Chanson (2014)	ADM measurement	0.5 to 1.3
	Richard & Gavrilyuk (2013)	numerical simulation	0.2 to 1.1
Large vortex advections	Chanson (2010)	visual observation	0.4 to 1.1
	Zhang et al. (2013)	visual observation	0.4 to 1.4

Note: ADM: acoustic displacement meter.

List of figure captions

Figure 1. Sketch of experimental channel and basic parameters of a hydraulic jump.

Figure 2. Double-tip conductivity phase-detection probes.
(a) Leading and trailing probe sensors separated with a longitudinal distance Δx
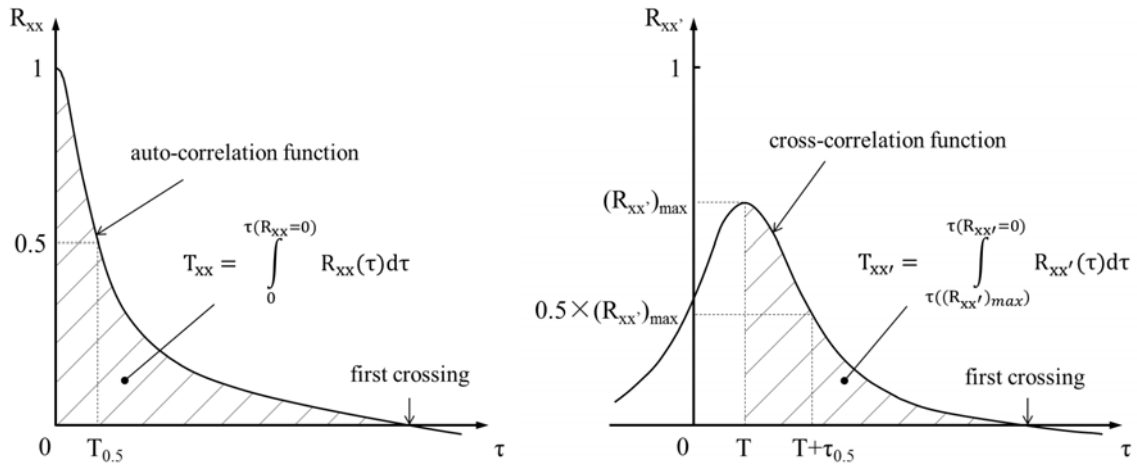(b) Leading sensors of side-by-side probes separated with a transverse distance Δz

Figure 3. Definition sketch of auto-correlation and cross-correlation functions of phase-detection probe signals.
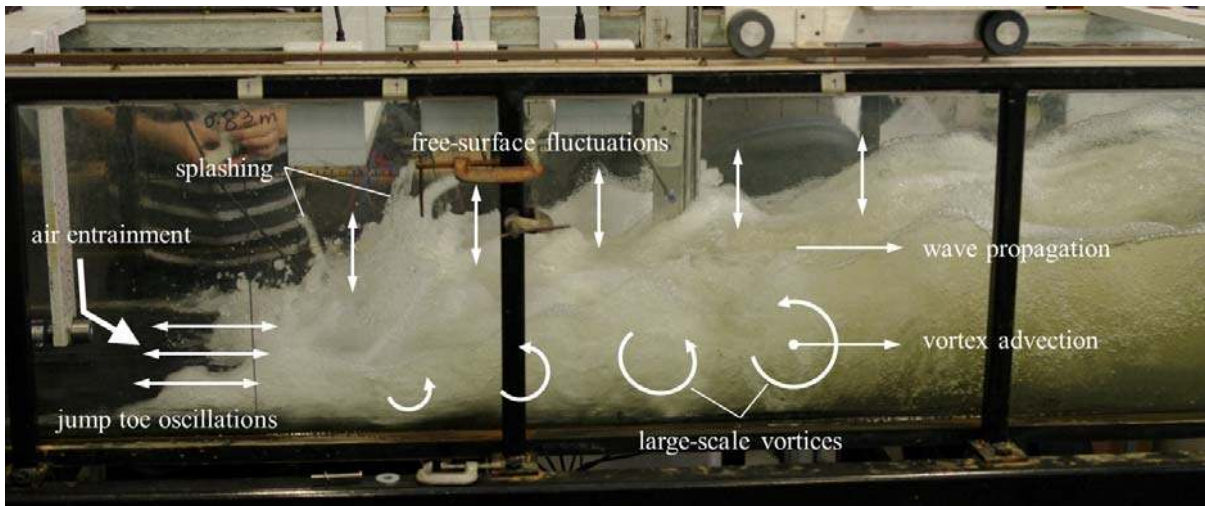
Figure 4. Macroscopic fluctuating motions in hydraulic jump roller – Flow conditions: $Q = 0.0347$ m^3/s, $d_1 = 0.0208$ m, $x_1 = 0.83$ m, $Fr_1 = 8.5$, $Re = 8.0 \times 10^4$.

Figure 5. Time-averaged void fraction and bubble count rate distributions in hydraulic jumps.
(a) Void fraction, $h/W = 0.06$
(b) Bubble count rate, $h/W = 0.06$
(c) Longitudinal decrease in local maximum void fraction and maximum bubble count rate in turbulent shear region, $h/W = 0.06$

Figure 6. Time-averaged air-water interfacial velocity and turbulence intensity distributions in hydraulic jumps.
(a) Interfacial velocity, $h/W = 0.06$
(b) Turbulence intensity, $h/W = 0.06$

Figure 7. Distributions of auto-correlation time scale T_{xx} and longitudinal/transverse cross-correlation time scales $T_{xx'}$ and T_{xz} – Flow conditions: $Q = 0.0333$ m^3/s, $d_1 = 0.02$ m, $x_1 = 0.83$ m, $Fr_1 = 7.5$, $Re = 6.6 \times 10^4$.

Figure 8. Distributions of turbulent length and time scales in longitudinal and transverse directions in hydraulic jumps – Flow conditions: $Q = 0.0333$ m^3/s, $d_1 = 0.02$ m, $x_1 = 0.83$ m, $Fr_1 = 7.5$, $Re = 6.6 \times 10^4$.
(a) Dimensionless advection length scale L_{xx}, longitudinal integral turbulent length scale L_X and transverse integral turbulent length scale L_Z
(b) Dimensionless longitudinal and transverse integral turbulent time scales T_X and T_Z

Figure 9. Power spectral density function of raw phase-detection probe signal – Flow conditions: $Q = 0.0333$ m^3/s, $d_1 = 0.02$ m, $x_1 = 0.83$ m, $Fr_1 = 7.5$, $Re = 6.6 \times 10^4$; $(x-x_1)/d_1 = 12.5$, $y/d_1 = 2.8$.

Figure 10. Decomposition of interfacial velocity in a vertical cross section of jump roller – Flow conditions: $Q = 0.0333$ m^3/s, $d_1 = 0.02$ m, $x_1 = 0.83$ m, $Fr_1 = 7.5$, $Re = 6.6 \times 10^4$; $(x-x_1)/d_1 = 12.5$.

Figure 11. Decomposition of turbulence intensity.
(a) Turbulence intensity for raw and filtered signals in a vertical cross section – Flow conditions: $Q = 0.0333$ m^3/s, $d_1 = 0.02$ m, $x_1 = 0.83$ m, $Fr_1 = 7.5$, $Re = 6.6 \times 10^4$; $(x-x_1)/d_1 = 8.35$.
(b) Comparison between turbulence intensities of raw signal and fast fluctuating signal component in the first half roller for all flow conditions

Figure 12. Decomposition of auto-correlation and longitudinal cross-correlation time scales in a vertical cross section – Flow conditions: $Q = 0.0333$ m^3/s, $d_1 = 0.02$ m, $x_1 = 0.83$ m, $Fr_1 = 7.5$, $Re = 6.6 \times 10^4$; $(x-x_1)/d_1 = 12.5$.

Figure 13. Decomposition of longitudinal advection length scale L_{xx} and integral turbulent length scale L_X – Flow conditions: $Q = 0.0333$ m^3/s, $d_1 = 0.02$ m, $x_1 = 0.83$ m, $Fr_1 = 7.5$, $Re = 6.6 \times 10^4$.
(a) Decomposition of longitudinal advection and integral turbulent length scales in a vertical cross section: $(x-x_1)/d_1 = 12.5$
(b) Longitudinal advection length scale and integral turbulent length scale for high-frequency signal components at different longitudinal positions
(c) Longitudinal distribution of maximum advection length scale and integral turbulent length scale for high-frequency signal components

Figure 14. Decomposition of longitudinal integral turbulent time scale T_X – Flow conditions: $Q = 0.0333$ m^3/s, $d_1 = 0.02$ m, $x_1 = 0.83$ m, $Fr_1 = 7.5$, $Re = 6.6 \times 10^4$.
(a) Decomposition of longitudinal integral turbulent time scales in a vertical cross section: $(x-x_1)/d_1 = 12.5$
(b) Longitudinal integral turbulent time scale for high-frequency signal components at different longitudinal positions – Compared with longitudinal cross-correlation time scales
(c) Longitudinal distribution of maximum and depth-averaged integral turbulent time scale for high-frequency signal components

Figure 1. Sketch of experimental channel and basic parameters of a hydraulic jump.
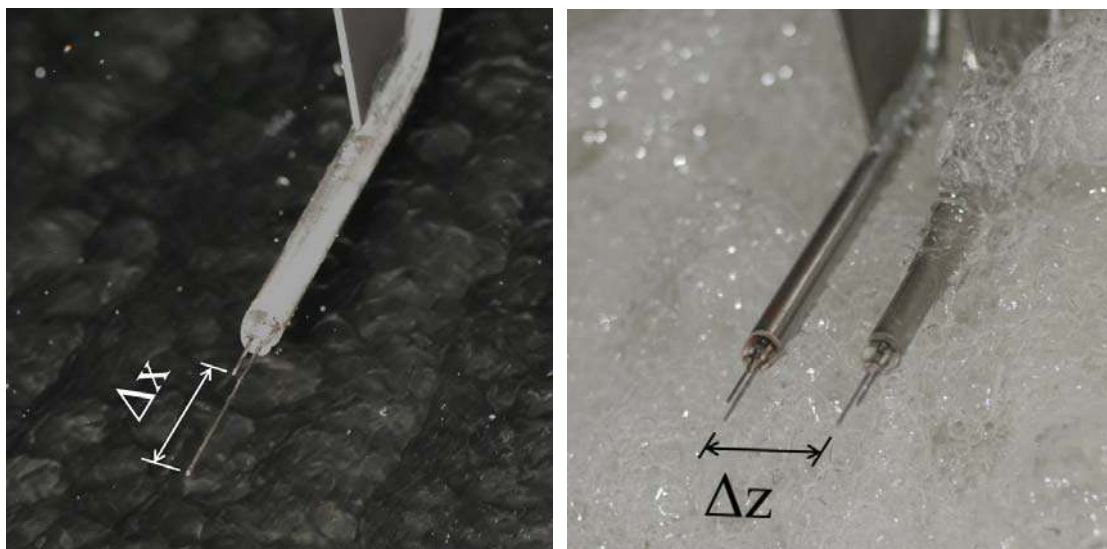
(a, left) Leading and trailing probe sensors separated with a longitudinal distance Δx
(b, right) Leading sensors of side-by-side probes separated with a transverse distance Δz
Figure 2. Double-tip conductivity phase-detection probes.

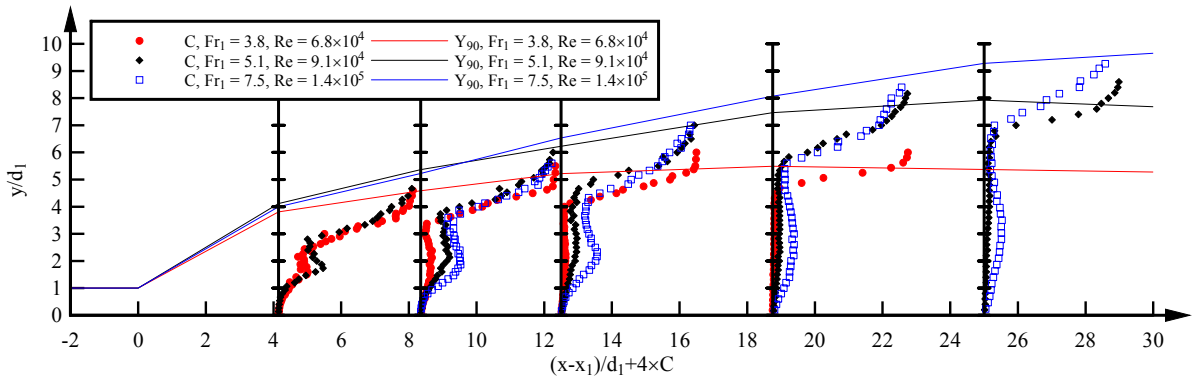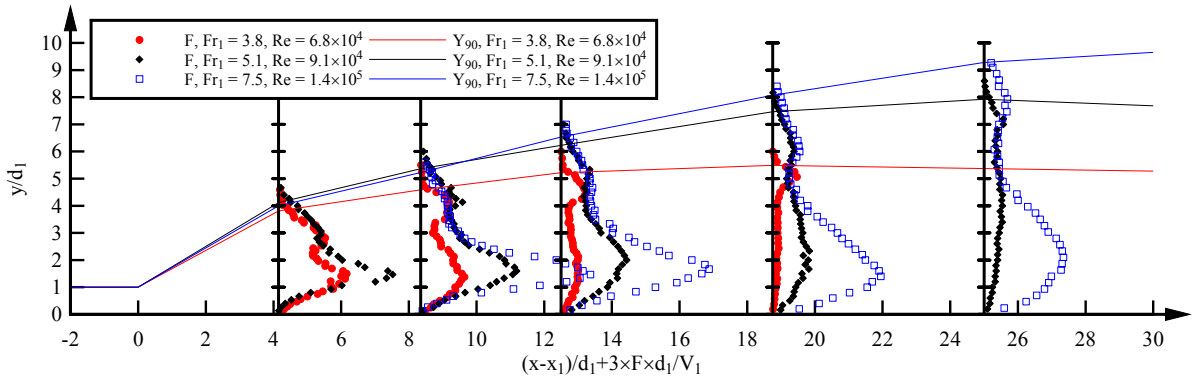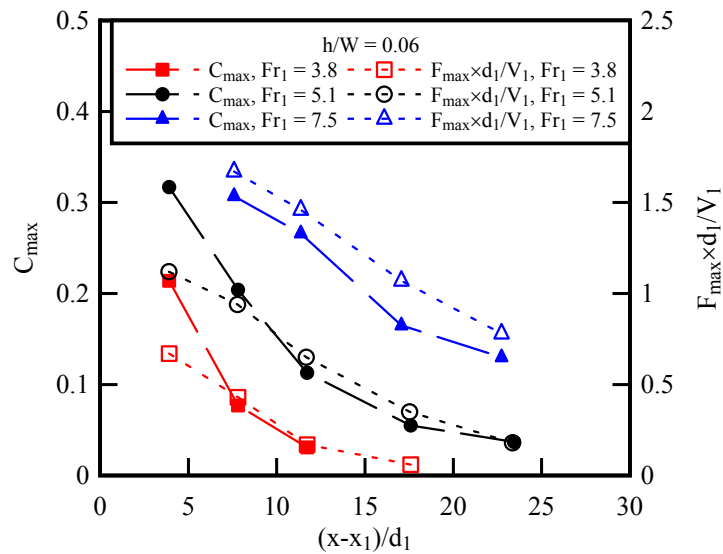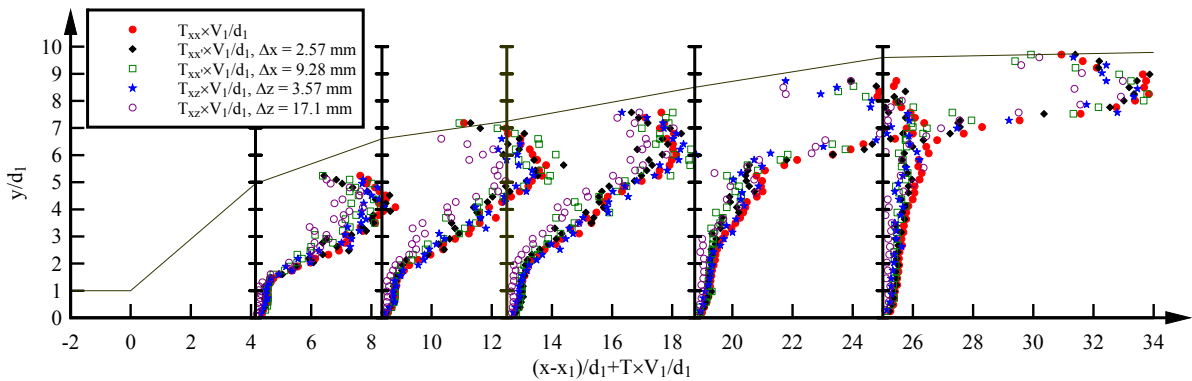Figure 3. Definition sketch of auto-correlation and cross-correlation functions of phase-detection probe signals.

Figure 4. Macroscopic fluctuating motions in hydraulic jump roller – Flow conditions: $Q = 0.0347$ m^3/s, $d_1 = 0.0208$ m, $x_1 = 0.83$ m, $Fr_1 = 8.5$, $Re = 8.0 \times 10^4$.

(a) Void fraction, h/W = 0.06

(b) Bubble count rate, h/W = 0.06

(c) Longitudinal decrease in local maximum void fraction and maximum bubble count rate in turbulent shear region, h/W = 0.06

Figure 5. Time-averaged void fraction and bubble count rate distributions in hydraulic jumps.
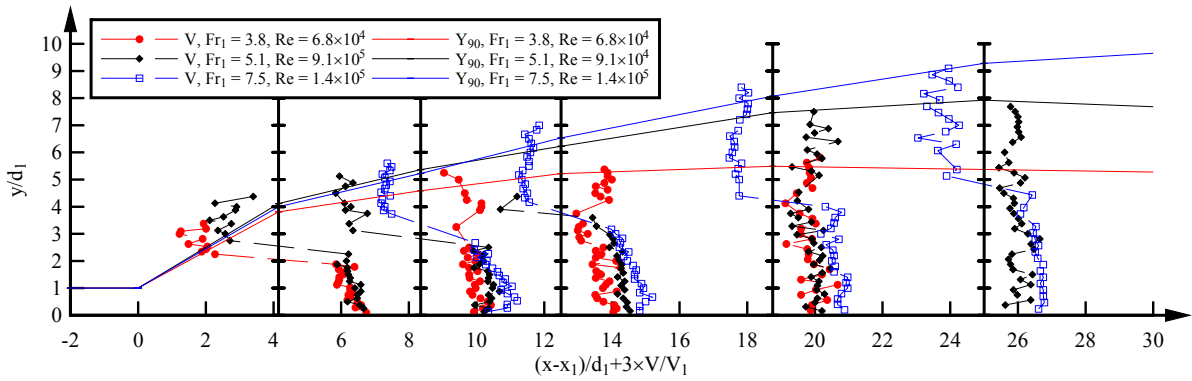
(a) Interfacial velocity, h/W = 0.06
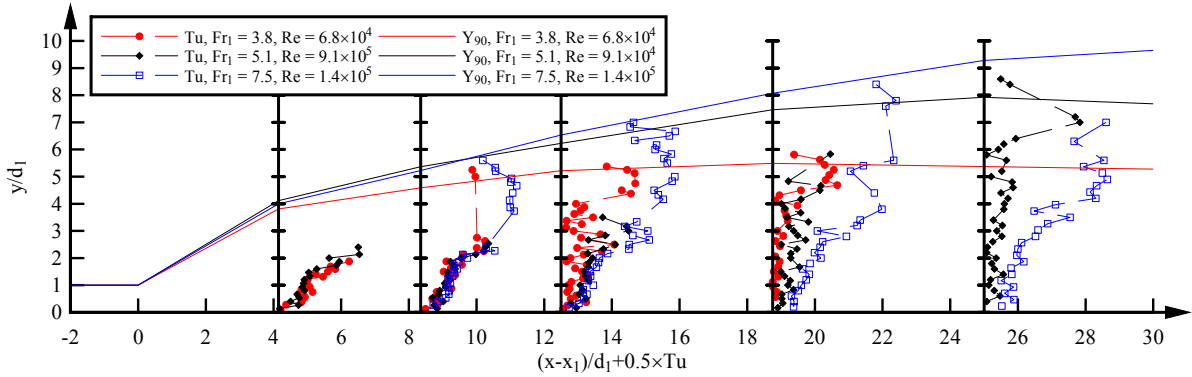
(b) Turbulence intensity, h/W = 0.06

Figure 6. Time-averaged air-water interfacial velocity and turbulence intensity distributions in hydraulic jumps.

Figure 7. Distributions of auto-correlation time scale T_{xx} and longitudinal/transverse cross-correlation time scales $T_{xx'}$ and T_{xz} – Flow conditions: Q = 0.0333 m^3/s, d_1 = 0.02 m, x_1 = 0.83 m, Fr_1 = 7.5, Re = 6.6×10^4.
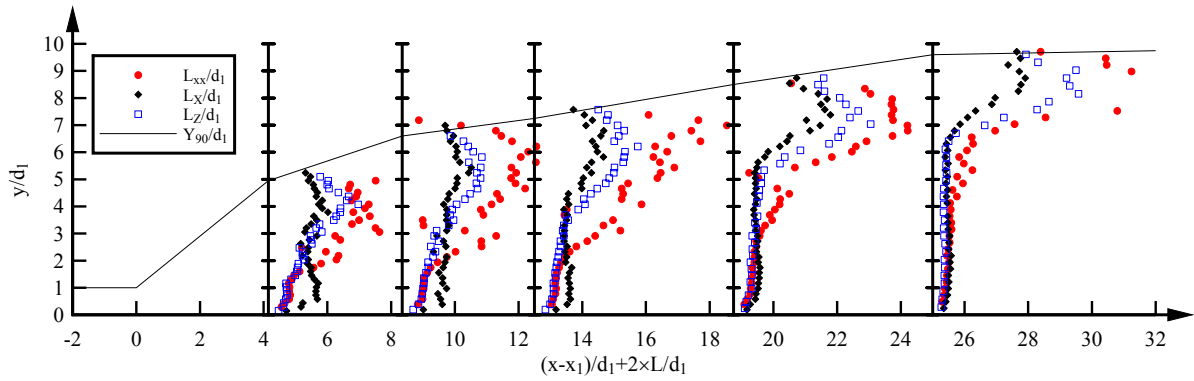
(a) Dimensionless advection length scale L_{xx}, longitudinal integral turbulent length scale L_X and transverse integral turbulent length scale L_Z
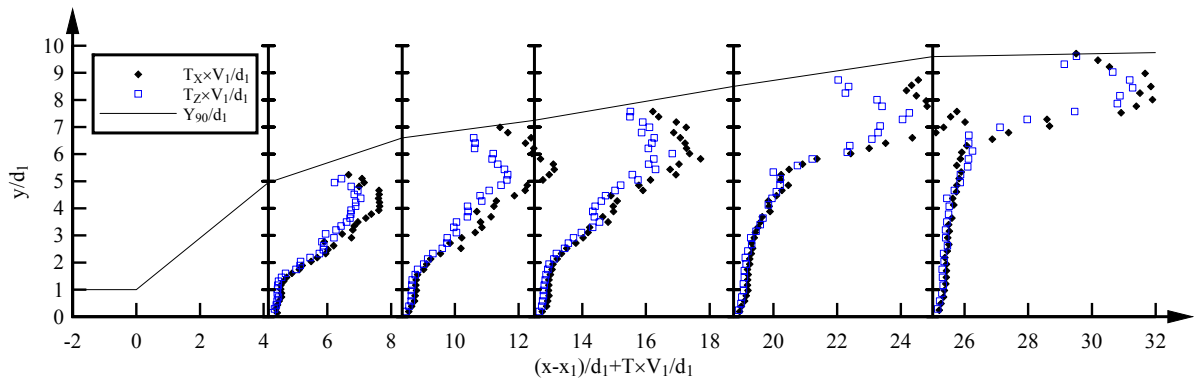
(b) Dimensionless longitudinal and transverse integral turbulent time scales T_X and T_Z

Figure 8. Distributions of turbulent length and time scales in longitudinal and transverse directions in hydraulic jumps – Flow conditions: $Q = 0.0333$ m^3/s, $d_1 = 0.02$ m, $x_1 = 0.83$ m, $Fr_1 = 7.5$, $Re = 6.6 \times 10^4$.
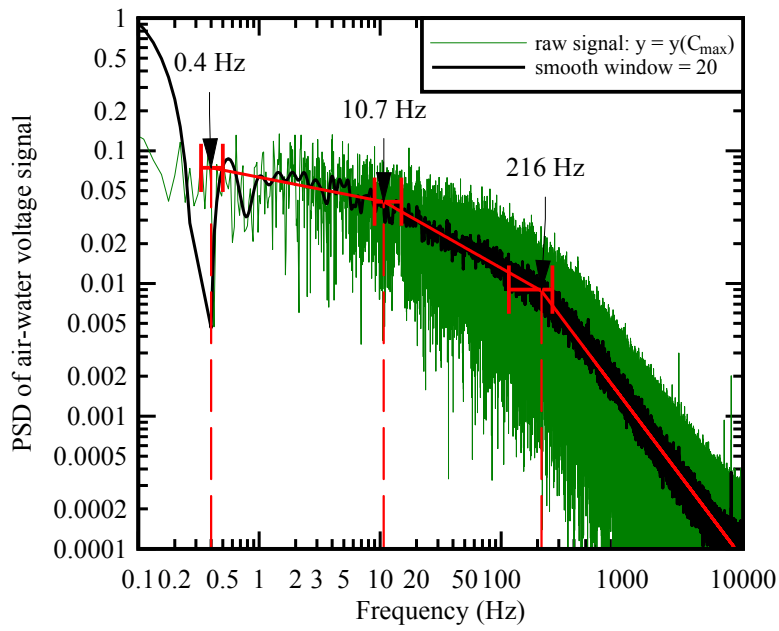
Figure 9. Power spectral density function of raw phase-detection probe signal – Flow conditions: $Q = 0.0333$ m^3/s, $d_1 = 0.02$ m, $x_1 = 0.83$ m, $Fr_1 = 7.5$, $Re = 6.6 \times 10^4$; $(x-x_1)/d_1 = 12.5$, $y/d_1 = 2.8$.
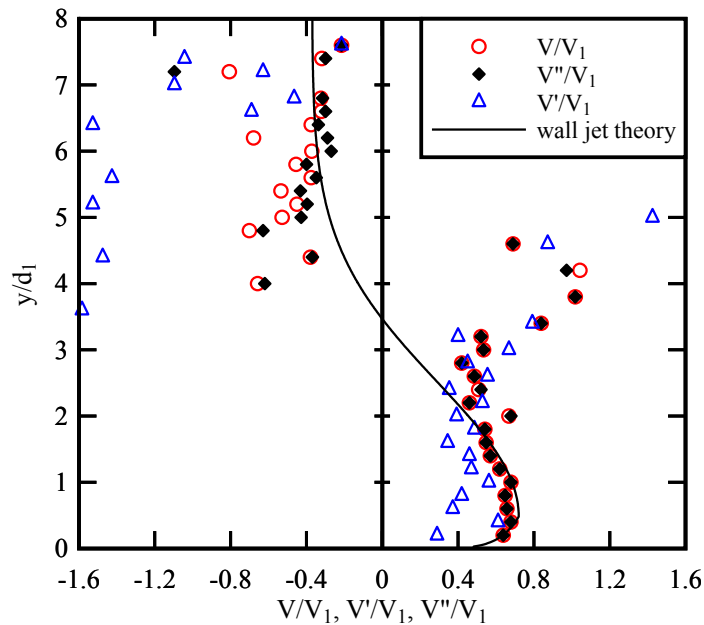
Figure 10. Decomposition of interfacial velocity in a vertical cross section of jump roller – Flow conditions: $Q = 0.0333$ m^3/s, $d_1 = 0.02$ m, $x_1 = 0.83$ m, $Fr_1 = 7.5$, $Re = 6.6 \times 10^4$; $(x-x_1)/d_1 = 12.5$.
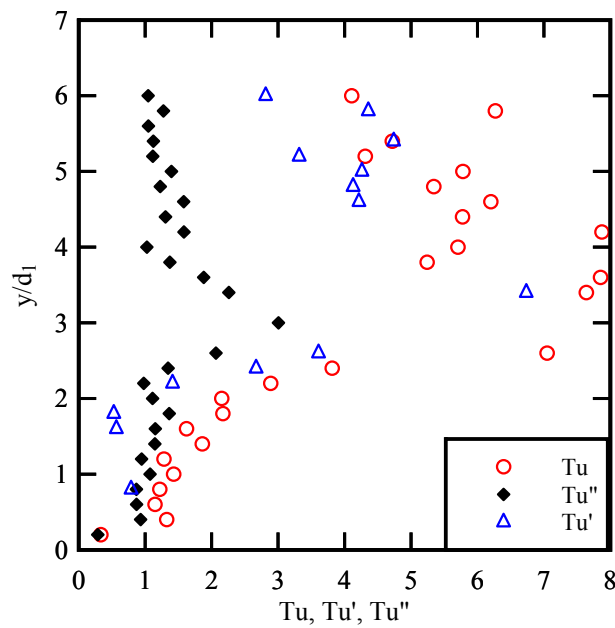
(a) Turbulence intensity for raw and filtered signals in a vertical cross section – Flow conditions: Q = 0.0333 m^3/s, d_1 = 0.02 m, x_1 = 0.83 m, Fr_1 = 7.5, Re = 6.6×10^4; (x-x_1)/d_1 = 8.35.
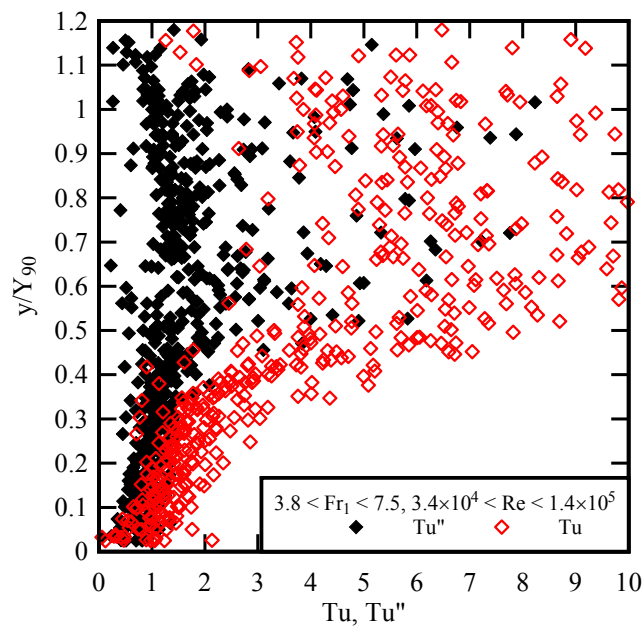
(b) Comparison between turbulence intensities of raw signal and fast fluctuating signal component in the first half roller for all flow conditions

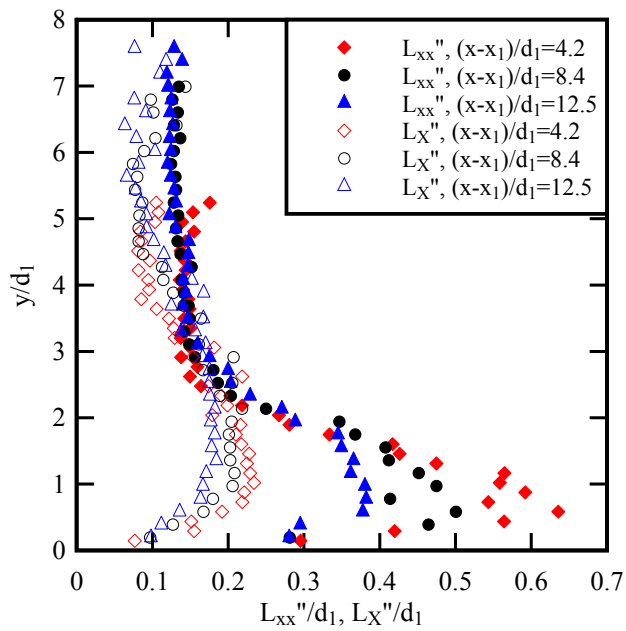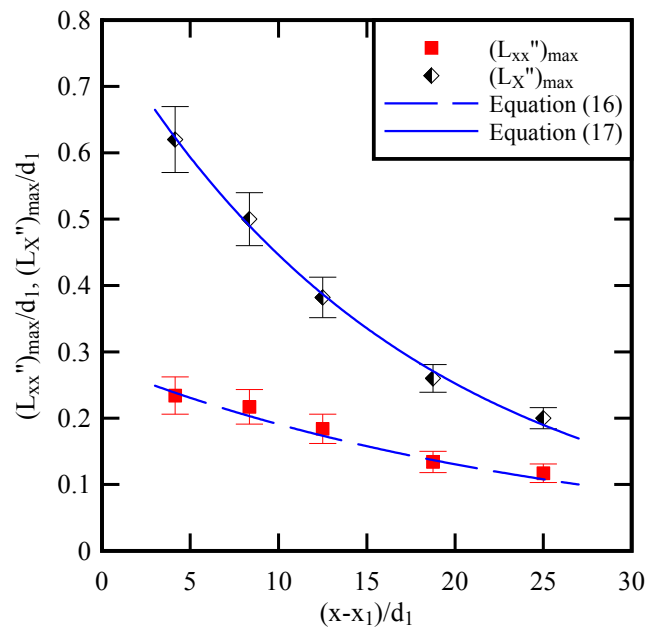Figure 11. Decomposition of turbulence intensity.
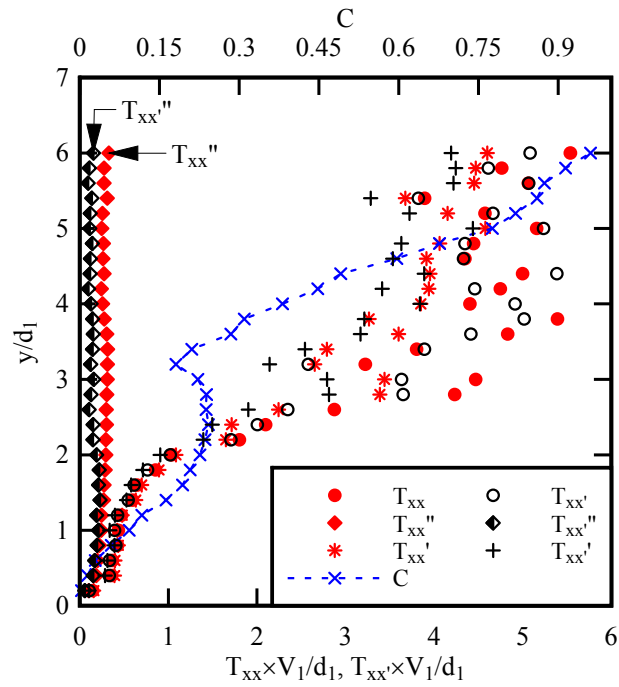
Figure 12. Decomposition of auto-correlation and longitudinal cross-correlation time scales in a vertical cross section – Flow conditions: Q = 0.0333 m^3/s, d_1 = 0.02 m, x_1 = 0.83 m, Fr_1 = 7.5, Re = 6.6×10^4; $(x-x_1)/d_1$ = 12.5.

(a) Decomposition of longitudinal advection and integral turbulent length scales in a vertical cross section: $(x-x_1)/d_1 = 12.5$
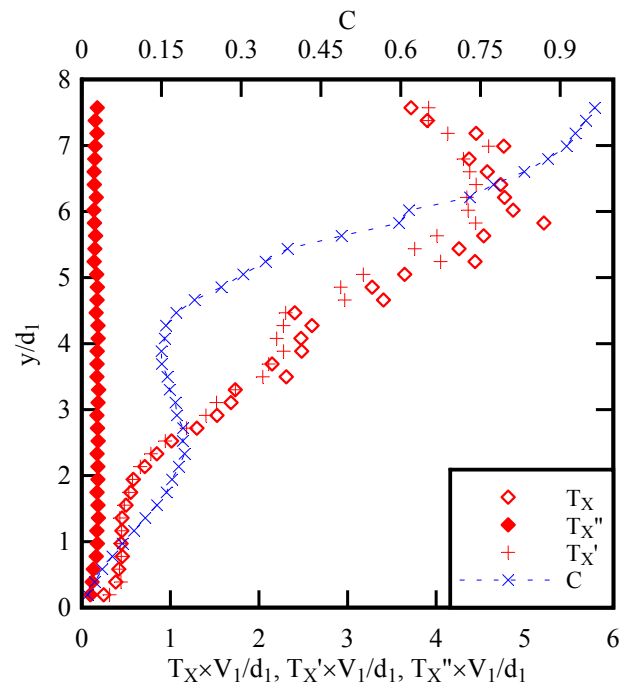

(b) Longitudinal advection length scale and integral turbulent length scale for high-frequency signal components at different longitudinal positions
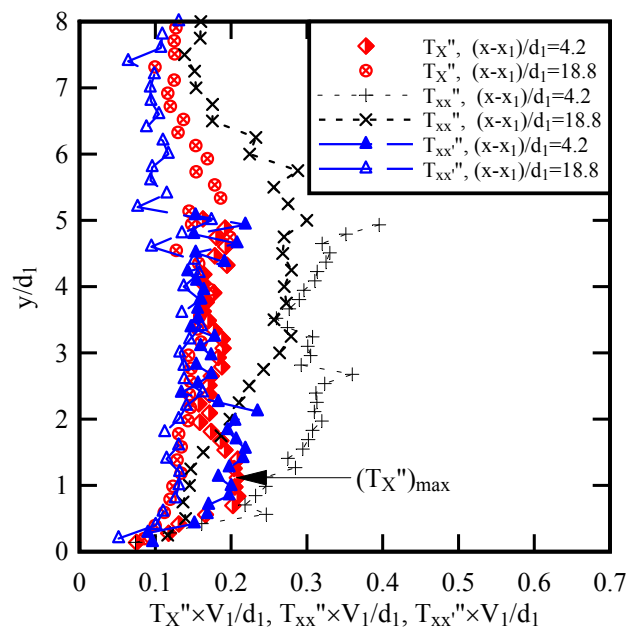
(c) Longitudinal distribution of maximum advection length scale and integral turbulent length scale for high-frequency signal components

Figure 13. Decomposition of longitudinal advection length scale L_{xx} and integral turbulent length scale L_X – Flow conditions: $Q = 0.0333$ m^3/s, $d_1 = 0.02$ m, $x_1 = 0.83$ m, $Fr_1 = 7.5$, $Re = 6.6 \times 10^4$.
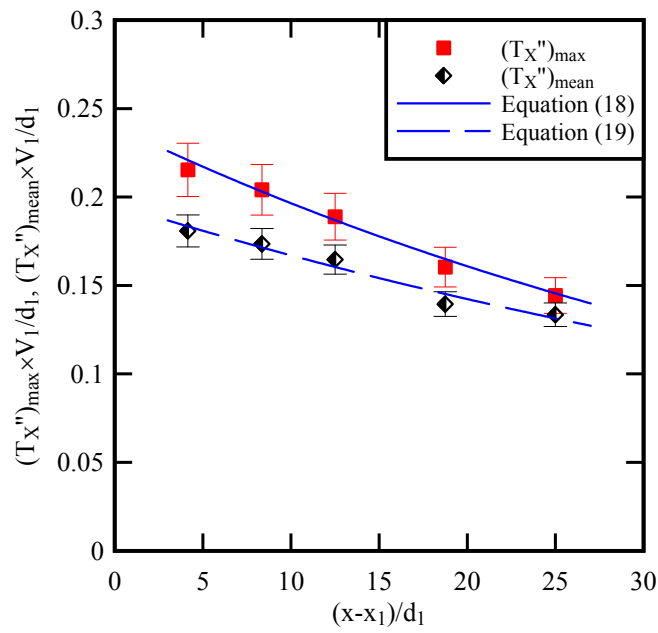
(a) Decomposition of longitudinal integral turbulent time scales in a vertical cross section: $(x-x_1)/d_1 = 12.5$

(b) Longitudinal integral turbulent time scale for high-frequency signal components at different longitudinal positions – Compared with longitudinal cross-correlation time scales

(c) Longitudinal distribution of maximum and depth-averaged integral turbulent time scale for high-frequency signal components

Figure 14. Decomposition of longitudinal integral turbulent time scale T_X − Flow conditions: Q = 0.0333 m^3/s, d_1 = 0.02 m, x_1 = 0.83 m, Fr_1 = 7.5, Re = 6.6×10^4.